

1 **Large variations in volcanic aerosol forcing efficiency due to eruption source**
2 **parameters and rapid adjustments**
3

4 **Lauren R. Marshall¹, Christopher J. Smith^{2,3}, Piers M. Forster², Thomas J. Aubry⁴,**
5 **Timothy Andrews⁵ and Anja Schmidt^{1,4}**
6

7
8 ¹Department of Chemistry, University of Cambridge, Cambridge, UK

9 ²Priestley International Centre for Climate, University of Leeds, Leeds, UK

10 ³International Institute for Applied Systems Analysis (IIASA), Laxenburg, Austria

11 ⁴Department of Geography, University of Cambridge, Cambridge, UK

12 ⁵Met Office Hadley Centre, Exeter, UK
13

14 Corresponding authors:

15 Lauren Marshall (lrm49@cam.ac.uk),

16 Anja Schmidt (anja.schmidt@ch.cam.ac.uk)
17
18
19

20 **Key Points:**
21

- 22 • The relationship between volcanic SAOD and ERF depends on the time after an
23 eruption, the eruption latitude and eruption season.
- 24 • Rapid adjustments reduce the volcanic forcing by an average of 20% predominantly
25 due to a positive shortwave cloud adjustment.
- 26 • We provide a range of global mean volcanic SAOD to global mean ERF conversions
27 dependent on eruption source parameters.

Abstract

The relationship between volcanic stratospheric aerosol optical depth (SAOD) and volcanic radiative forcing is key to quantify volcanic climate impacts. In their fifth assessment report, the Intergovernmental Panel on Climate Change used one scaling factor between volcanic SAOD and volcanic forcing based on climate model simulations of the 1991 Mt. Pinatubo eruption, which may not be appropriate for all eruptions. Using a large-ensemble of aerosol-chemistry-climate simulations of eruptions with different sulfur dioxide emissions, latitudes, emission altitudes and seasons, we find that the effective radiative forcing (ERF) is on average 20% less than the instantaneous radiative forcing, predominantly due to a positive shortwave cloud adjustment. In our model, the volcanic SAOD-ERF relationship is non-unique and varies widely depending on time since an eruption, eruption latitude and season due to differences in aerosol dispersion and incoming solar radiation. Our revised SAOD-ERF relationships suggest that volcanic forcing has been previously overestimated.

Plain Language Summary

Powerful explosive volcanic eruptions inject sulfur gases high into the atmosphere where they form a layer of sulfate aerosol particles that scatter sunlight back into space, decrease the transparency of the atmosphere and cause surface cooling. The amount of sunlight that is scattered depends on the location of the layer of particles and particle size. We have used a complex climate model to quantify how eruptions of different magnitudes and occurring in different seasons and locations, may affect the climate. We find that the relationship between the transparency of the atmosphere and the resulting climatic impact caused by volcanic sulfate aerosol particles depends on the spread of the aerosol and therefore the time since the eruption, the eruption location and the season. Our simulations also show that the eruptions reduce the cooling effect of clouds, which reduces the overall effectiveness of volcanoes at cooling the Earth's surface.

1 Introduction

Volcanic sulfate aerosol, formed in the stratosphere following the release of sulfur dioxide (SO_2) during explosive volcanic eruptions, scatters incoming shortwave radiation and absorbs longwave radiation, which leads to surface cooling that has defined the natural variability in climate over the last millennium (Myhre et al., 2013; Schurer et al., 2013; Sigl et al., 2015).

Stratospheric aerosol optical depth (SAOD), which is a measure of the opacity of the stratosphere, is a key property used to estimate the radiative forcing of an eruption. The relationship between the two is a measure of how effective the volcanic aerosol is at forcing climate change and can be used to compare volcanic forcing to other climate forcing agents (Hansen et al., 2005). Traditionally, a constant relationship between SAOD and volcanic forcing is assumed; in the Fifth Assessment Report from the Intergovernmental Panel on Climate Change (IPCC AR5, Myhre et al., 2013), a forcing scaling factor of -25 W m^{-2} per unit change of volcanic SAOD is used. This factor was based on simulations of the 1991 eruption of Mt. Pinatubo in the Goddard Institute for Space Studies (GISS) model E (Hansen et al., 2005). Energy balance models and simple climate models (e.g., Haustein et al., 2019; Smith et al., 2018a), which continue to underpin IPCC calculations of radiative forcing and are used in studies that assess the 1.5°C target of the Paris Agreement (e.g., Smith et al., 2019) remain dependent on such conversions. Furthermore, studies that estimate forcing from volcanism on geological timescales (e.g., Landwehrs et al., 2020) rely on using scaling factors to convert SAOD to volcanic forcing.

74 The use of a single scaling factor is problematic for two main reasons. Firstly, the
 75 relationship between SAOD and radiative forcing is dependent on several factors such as the
 76 cloud cover, surface albedo and insolation (e.g., Andersson et al., 2015). Consequently, the
 77 relationship may be dependent on the eruption latitude, the magnitude of the SO₂ emission,
 78 emission altitude, and the eruption season as these parameters dictate the location and amount
 79 of aerosol that forms (Marshall et al., 2019; Toohey et al., 2011; Toohey et al., 2013), and
 80 may differ from that after 1991 Mt. Pinatubo. Secondly, the relationship between SAOD and
 81 volcanic forcing depends on how the radiative forcing is calculated; whether this is the
 82 instantaneous radiative forcing (IRF) at the tropopause or top of atmosphere (TOA), a
 83 stratospherically-adjusted radiative forcing that accounts for changes in stratospheric
 84 temperature (e.g., the IPCC AR5 -25 W m⁻² per unit SAOD value), or the effective radiative
 85 forcing (ERF), which accounts for additional radiative effects (termed rapid adjustments) due
 86 to changes in the surface land temperature, surface albedo, the tropospheric temperature,
 87 water vapor and clouds (Forster et al., 2013; Smith et al., 2018b). Studies have found that
 88 when rapid adjustments are included, the total volcanic radiative forcing for large-magnitude
 89 eruptions (i.e., 1991 Mt. Pinatubo magnitude) is around 20% weaker than that used in the
 90 IPCC AR5, due to positive aerosol-cloud interactions that reduce the magnitude of the
 91 negative radiative forcing (Gregory et al., 2016; Larson & Portmann, 2016; Schmidt et al.,
 92 2018). However, these studies are based on relatively few historical eruptions, and a
 93 systematic investigation into the effectiveness of volcanic forcing across eruptions of
 94 different magnitude and with different source parameters has not been conducted.

95 **2 Methods**

96 **2.1 Aerosol-chemistry-climate model simulations**

97 We have used aerosol-chemistry-climate model simulations of a wide range of
 98 eruptions that inject SO₂ into the stratosphere to investigate the relationship between SAOD
 99 and the ERF. The ERF is the best indication of the resulting temperature response of a
 100 particular forcing agent (Forster et al., 2016; Myhre et al., 2013; Sherwood et al., 2015).
 101 Simulations were run using the UM-UKCA interactive stratospheric aerosol model, which
 102 includes the HadGEM3-GA4 climate model (Walters et al., 2014), the GLOMAP-mode
 103 prognostic aerosol scheme (Mann et al., 2010) and interactive whole-atmosphere chemistry
 104 as described in Marshall et al. (2019). Volcanic eruptions are simulated by adding an
 105 emission of SO₂ so that changes in aerosol number, mass and size are accounted for when
 106 calculating SAOD. Prescribed SAOD datasets derived from ice-core-records of sulfate
 107 deposition (Crowley & Unterman, 2013; Gao et al., 2008; Toohey & Sigl, 2017) used in
 108 previous modelling studies are uncertain and do not include many microphysical and
 109 dynamical effects of the aerosol on the resulting optical properties (Toohey et al., 2016). Our
 110 simulations were free-running so that aerosol perturbations can feed back onto the model's
 111 dynamics, and atmosphere-only with prescribed climatological sea surface temperatures
 112 (SSTs) that allow the ERF to be diagnosed (Forster et al., 2016; Smith et al., 2018b). ERF is
 113 calculated as the difference in the net (shortwave + longwave) all-sky top-of-atmosphere
 114 energy imbalance between the simulation with the volcanic SO₂ emission and a control
 115 simulation with no eruption (all other aspects of the two model simulations remain the same).
 116 Similarly, we examine the change in SAOD at 550 nm between the two simulations (the
 117 volcanic SAOD). The calculation of IRF is outlined in section 2.2.

118 We simulated 82 explosive eruptions with different values of the SO₂ emission,
 119 eruption latitude and the emission height, termed 'eruption source parameters', and with half
 120 of the eruptions occurring on the 1st of January, and half with the eruption occurring on the 1st
 121 of July (with the same combinations of the eruption source parameters). The July simulations

122 are presented in Marshall et al. (2019) and were repeated for this study for the 1st January
123 eruption start date. The value of each eruption source parameter in each simulation was
124 determined using a Latin Hypercube design as described in Marshall et al. (2019) (see their
125 Figure 1), with SO₂ emissions ranging between 10 and 100 Tg of SO₂, eruption latitude
126 between 80°S and 80°N, and a 3-km-deep emission column ranging between 15-18 km and
127 25-28 km leading to very good coverage of the three-dimensional parameter space. The SO₂
128 emissions range from that of 1991 Mt. Pinatubo, estimated to be between 10 and 20 Tg (Guo
129 et al., 2004; Timmreck et al., 2018), to 1815 Mt Tambora (~60 Tg; Zanchettin et al., 2016)
130 and approaching that of 1257 Samalás (~119 Tg; Toohey & Sigl, 2017). Each simulation was
131 run for 38 months following the eruption and was initialized during the easterly phase of the
132 Quasi Biennial Oscillation. We do not run additional ensemble members for each eruption
133 but group the eruptions into subsets in which we analyze average responses focusing on
134 annual and global means that have a low sensitivity to meteorological variability. This is
135 supported by previous UM-UKCA ensemble members of the large-magnitude (~60 Tg SO₂)
136 Mt. Tambora eruption (Zanchettin et al., 2016, Marshall et al., 2018) in which global mean
137 SAOD was very similar.

138 **2.2 Diagnosing instantaneous radiative forcing and rapid adjustments**

139 For each of the 82 eruptions we calculate rapid adjustments using the radiative kernel
140 method (Shell et al., 2008; Soden et al., 2008). Differences between simulated responses of
141 surface temperature, atmospheric temperature, specific humidity and surface albedo are taken
142 from each eruption and its corresponding control (January or July) and multiplied by the
143 radiative kernel based on the HadGEM3-GA7.1 climate model (Smith et al., 2020). The
144 kernel converts a perturbation in atmospheric state to a top-of-atmosphere radiative flux
145 based on the latitude, longitude, height and month of the perturbation.

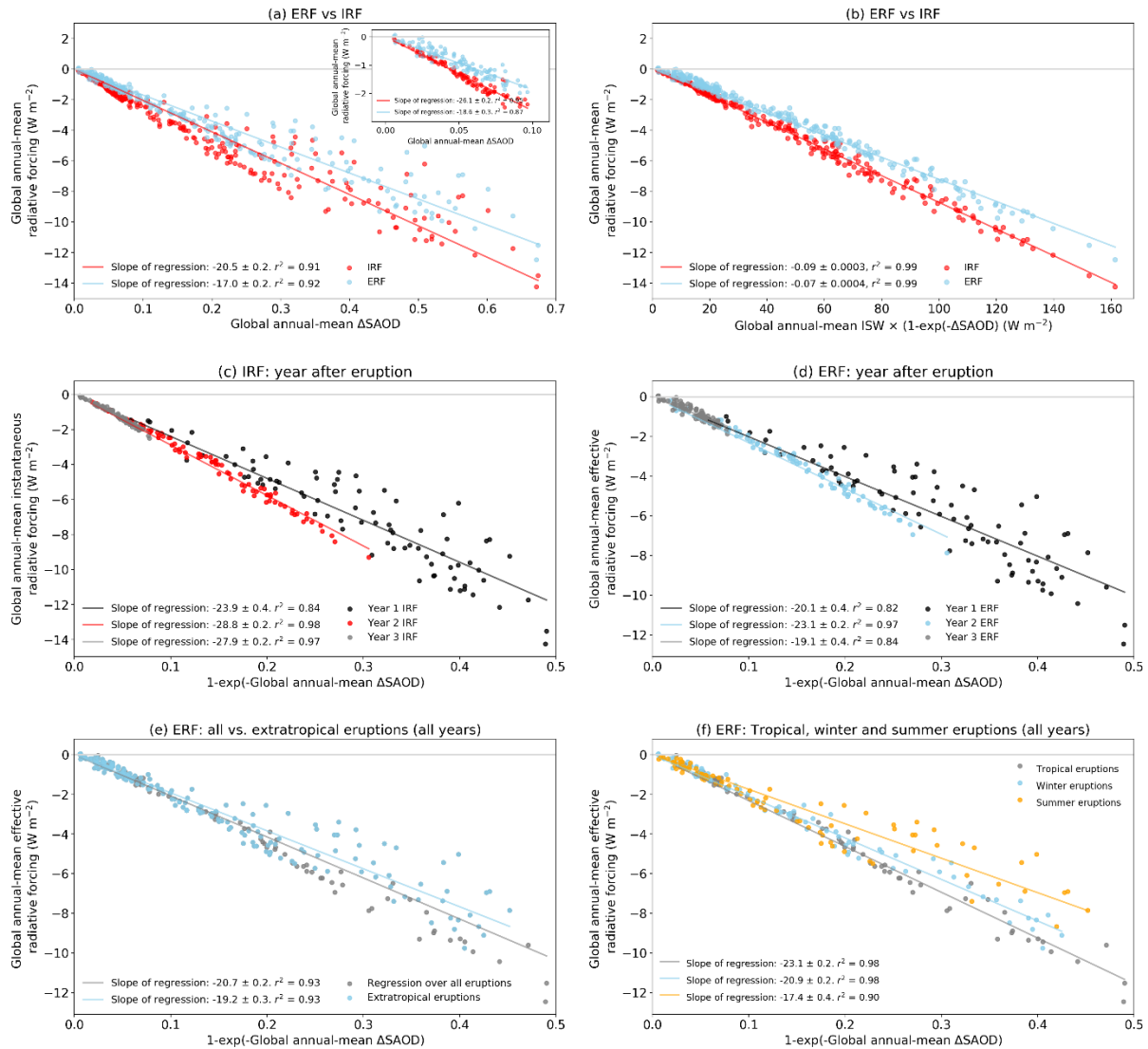
146 For shortwave (SW) cloud rapid adjustments we use the Approximate Partial
147 Radiative Perturbation (APRP) technique (Taylor et al., 2007), which approximates the
148 scattering and absorption of SW radiation through the atmosphere by clouds without
149 specialized model diagnostics. Longwave (LW) cloud rapid adjustments are estimated by
150 substituting cloud fields from each experiment into the base climatology, and vice versa,
151 running both configurations through the SOCRATES offline radiative transfer code (Edwards
152 & Slingo, 1996; Manners et al., 2015), which is the radiation module used in UM-UKCA,
153 and taking the average of the “forward” and “reverse” substitutions. This offline substitution
154 method is akin to a partial radiative perturbation (Wetherald & Manabe, 1988). The IRF is
155 then estimated as the difference between the ERF and the sum of all rapid adjustments (Smith
156 et al., 2018b).

157

158 **3 Results and Discussion**159 **3.1 The relationship between global annual-mean volcanic SAOD and radiative forcing**

160

161



162

163 **Figure 1.** (a) Regression of global annual-mean volcanic SAOD (at 550 nm) against the IRF
 164 (red) and ERF (blue) for all 82 simulations. The scatter points show the two quantities in each
 165 of the three years after each eruption (82 simulations x 3 years giving 246 data points). The
 166 inset shows the regression for SAOD values less than 0.1, upon which the IPCC AR5 scaling
 167 factor is based. (b) Global annual mean of 1-exp(-SAOD) multiplied by the incoming
 168 shortwave radiation (ISW), against IRF and ERF. (c) 1-exp(-SAOD) against IRF for each
 169 year after the eruption. (d) As c, but for ERF. (e) As d, but for all and extratropical eruptions
 170 for all years. (f) As d, but for tropical, winter and summer eruptions for all years. The IRF is
 171 shown in Figure S1.

172

173 Figure 1 shows a series of different regressions to explore the relationship between
 174 volcanic SAOD and volcanic radiative forcing. To compare directly with previous
 175 conversions, we show first in Figure 1a the global annual-mean volcanic SAOD regressed
 176 against both the IRF and ERF for the three years following each eruption across all 82

177 simulations. The slope of each regression line gives the scaling factor in terms of radiative
 178 forcing (IRF or ERF) per unit of SAOD. Across all eruptions the IRF is stronger than the
 179 ERF, demonstrating that total rapid adjustments are positive, acting to reduce the magnitude
 180 of the forcing, in agreement with previous studies (Gregory et al., 2019; Gregory et al., 2016;
 181 Hansen et al., 2005; Larson & Portmann, 2016; Schmidt et al., 2018). We explore the rapid
 182 adjustments further in section 3.2. Consequently, the IRF scaling factor is larger than the ERF
 183 scaling factor, estimated from the regression slopes as $-20.5 \pm 0.2 \text{ W m}^{-2}$ and $-17.0 \pm 0.2 \text{ W}$
 184 m^{-2} , respectively.

185 The linear regression fit for IRF over small SAOD values (<0.1 , Figure 1a inset: -26.1
 186 $\pm 0.2 \text{ W m}^{-2}$ per unit SAOD) can be directly compared to the IPCC AR5 scaling factor, which
 187 is derived from SAOD values also less than ~ 0.1 . Although IPCC AR5 uses the -25 W m^{-2}
 188 per unit SAOD factor, additional simulations run with the GISS model E for 1991 Pinatubo
 189 using fixed SSTs, produce a scaling factor of -26 W m^{-2} per unit SAOD
 190 (<https://data.giss.nasa.gov/modelforce/strataer/>). Because we also use fixed SSTs in our
 191 model simulations, we subsequently use the -26 W m^{-2} factor to compare our results to IPCC
 192 AR5 (following Schmidt et al., 2018). Our scaling for IRF over small SAOD values is
 193 consequently identical to that of IPCC AR5. Our scaling for the ERF and small SAOD values
 194 ($-18.6 \pm 0.3 \text{ W m}^{-2}$ per unit SAOD) is smaller than that calculated by Schmidt et al. (2018)
 195 using CESM1-WACCM simulations when regressing for the years 1982-1985 and 1991-1994
 196 characterized by the eruptions of El Chichón and Mt. Pinatubo and SAOD also less than ~ 0.1
 197 ($-21.5 \pm 1.1 \text{ W m}^{-2}$ per unit SAOD; blue line in their Figure 6). This is because we do not
 198 include an intercept in our fits so that a zero change in SAOD does not result in a radiative
 199 forcing. If we do include an intercept our scaling factor is $-20.9 \pm 0.7 \text{ W m}^{-2}$ per unit SAOD,
 200 which compares very well to Schmidt et al. (2018).

201 The spread around the regression line in Figure 1a collapses if we account for the
 202 spatial distribution of the sulfate aerosol and the incoming shortwave radiation (ISW). We
 203 first transform the globally and temporally-resolved SAOD to $1 - e^{-\text{SAOD}}$ (based on a simple
 204 application of the Beer-Lambert law) and multiply by the ISW before taking the global
 205 annual-mean (Figure 1b). To explore the driving factors of the reduction in this spread,
 206 Figures 1c-f show the eruptions categorized according to the year after eruption, eruption
 207 latitude and eruption season.

208 We find that the conversion between SAOD and ERF depends on the time after an
 209 eruption, eruption latitude and eruption season because of differences in the aerosol
 210 distribution and the magnitude of the incoming solar radiation that result in differences in the
 211 magnitude of the IRF. Forcing per unit of SAOD is weaker in year 1 than in years 2 and 3
 212 with most of the spread in the datapoints arising from year 1 (Figures 1c-d). Forcing per unit
 213 of SAOD is stronger for tropical eruptions (between 20°S and 20°N) than extratropical
 214 eruptions and stronger for winter eruptions than summer eruptions (Figures 1e-f).

215 In the first year following extratropical eruptions, the aerosol is spatially concentrated
 216 in the hemisphere in which it was injected and the IRF depends on the strength of the
 217 insolation. This results in a dependency on the eruption season as there is more insolation in
 218 the summer hemisphere than the winter hemisphere. Because it takes around 6 months for the
 219 aerosol to reach peak burden in our simulations, it is the winter eruptions where more aerosol
 220 coincides with high summer insolation resulting in a higher forcing. Zonal mean SAOD and
 221 ERF alongside the ISW are shown for each eruption category in Figures S2-4. In the second
 222 year after the eruption the aerosol has dispersed more widely, driven by large-scale
 223 circulation timescales, which results in a higher global mean albedo for the same global mean
 224 SAOD, resulting in a larger global mean forcing per unit of SAOD (but both the SAOD and

225 forcing has reduced by year 2). In addition, depending on the eruption season and latitude, the
226 aerosol may spread to areas with higher ISW, which further enhances the global mean forcing
227 per unit of SAOD. By the third year the aerosol has been largely removed. For tropical
228 eruptions, the aerosol spreads to both hemispheres and is longer-lived as well as coinciding
229 with high tropical insolation resulting in higher SAOD and higher forcing. The dependency
230 on latitude and season is therefore mainly present in the first year after the eruption.

231 The slope of the regressions in Figures 1c-f can be used to convert global annual-
232 mean SAOD (in the form of $1 - e^{-SAOD}$) to ERF depending on eruption source parameters.
233 Transforming SAOD to $1 - e^{-SAOD}$ removes some of the non-linearity in the data and is chosen
234 here since it is a physically-based quantity that relates to forcing. These conversions are listed
235 in Table S1. Although the global mean conversions cannot explain all the variability
236 discussed above, global annual-mean SAOD remains the most used metric in simple climate
237 models. Importantly, the large range in conversions across the different categories of
238 eruptions illustrates that the SAOD to ERF relationship is non-unique and that the current
239 practice of using a single scaling factor to convert between SAOD and forcing is not
240 appropriate for every eruption.

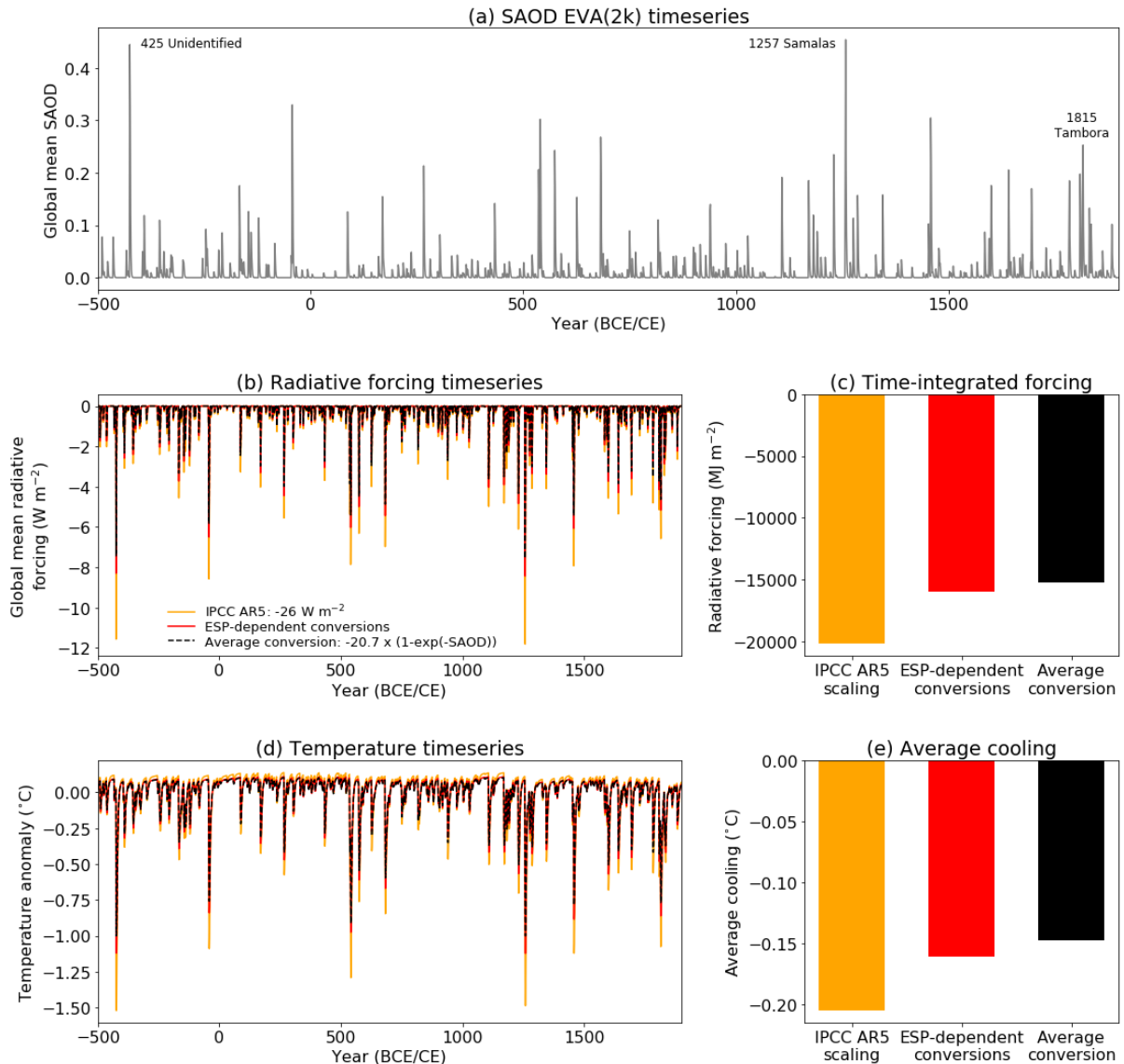
241 Using the latest reconstruction of global annual-mean volcanic SAOD for the period
242 500 BCE to 1900 CE (EVA(2k): Toohey & Sigl 2017, Figure 2a), we have calculated three
243 different volcanic radiative forcing time-series: 1) By multiplying the global annual-mean
244 SAOD timeseries by the IPCC AR5 factor (-26 W m^{-2}). 2) Converting the global annual-
245 mean SAOD using the all-eruption average relationship we derived here (Figure 1e),
246 $ERF = -20.7 \times (1 - e^{-SAOD})$. 3) Converting the global annual-mean SAOD using our
247 eruption source parameter (ESP) dependent relationships (Table S1, Figure 1e-f) for tropical,
248 extratropical (if season is unknown), winter and summer eruptions depending on the latitude
249 and season of each eruption from the reconstruction. In this example, annual SAOD values
250 are calendar years. We do not convert EVA SAOD depending on the year after the eruption
251 as the ESP dependent relationships account for a large amount of the variability in the SAOD
252 to ERF conversion (Figure 1f) and the temporal evolution in the EVA reconstruction is based
253 on a simple box model with decay timescales that are different to aerosol-climate models that
254 explicitly account for volcanic SO_2 emissions (Aubry et al., 2020; Zanchettin et al. 2016).

255 The total time-integrated forcing between 500 BCE and 1900 CE using our ESP-
256 dependent conversions is 79% of the total time-integrated forcing when using the IPCC AR5
257 factor (-15977 MJ m^{-2} vs. -20191 MJ m^{-2}). When using the all-eruption average conversion,
258 the total time-integrated forcing is only 75% of the IPCC AR5 total (-15233 MJ m^{-2}) (Figures
259 2b and c). Consequently, around 20-25% less energy has been lost from the climate system
260 due to volcanic radiative forcing between 500 BCE and 1900 CE than implied by the IPCC
261 AR5.

262 Figure 2d shows global annual-mean surface temperature anomalies calculated in a
263 simple climate model, FaIR (Finite Amplitude Impulse-Response simple climate-carbon-
264 cycle model) v1.4 (Millar et al., 2017; Smith et al., 2018a), forced with the three volcanic
265 forcing timeseries from Figure 2b. No other forcing agents are used such that the temperature
266 response is that from volcanic forcing only. To ensure that the climate is in balance long-term
267 and to avoid a long-term cooling trend, the volcanic forcing input to FaIR in Figure 2b is
268 adjusted such that the mean forcing over the timeseries is zero (resulting in small positive
269 ERF in volcanically-quiescent years). The simulated peak global mean surface cooling differs
270 by up to $0.4\text{-}0.5^\circ\text{C}$ for the largest eruptions depending on the conversion used, demonstrating
271 that there are substantial uncertainties on the magnitude of past volcanic climate impacts. For
272 example, using the IPCC AR5 scaling, simulated peak global mean cooling following the

273 1257 Samalas eruption is 1.5°C (occurring in 1259) and for 1815 Mt. Tambora is -1.1°C
 274 (occurring in 1816). Using the average conversion, the peak cooling is -1.0°C following
 275 Samalas and -0.8°C following Tambora. For the ESP-dependent conversions, the peak
 276 cooling is -1.1°C for Samalas and -0.9°C for Tambora. These predicted surface temperature
 277 changes fall within the range of estimated cooling from proxy reconstructions; tree-ring
 278 reconstructions of NH extratropical summer land cooling following 1257 Samalas and 1815
 279 Mt. Tambora eruptions are -0.8°C to -1.3°C (Stoffel et al., 2015). A comparison of the
 280 average global-mean cooling resulting from applying the different conversions across the
 281 whole timeseries is shown in Figure 2e.

282



283

284 **Figure 2.** (a) Global annual-mean volcanic SAOD timeseries from the EVA(2k)
 285 reconstruction (calendar years), which does not include background sulfur emissions so that
 286 SAOD represents the change due to volcanic eruptions only (b) Volcanic forcing calculated
 287 from the SAOD using the IPCC AR5 scaling factor (orange), eruption source parameter
 288 (ESP) dependent conversions (Table S1) (red) and the all-eruption average conversion
 289 (black). (c) Time-integrated forcing from 500 BCE to 1900 CE for the three conversion
 290 methods. (d) Global annual-mean surface temperature anomalies (relative to the 2400-year

291 average from each timeseries) calculated in a simple climate model (FaIR) for each volcanic
 292 forcing timeseries. (e) The average cooling for temperature anomalies less than 0 for the three
 293 conversion methods.

294

295 **3.2 The role of rapid adjustments**

296 In all simulations, the total global-mean rapid adjustments integrated over the duration
 297 of the simulations are positive and therefore the ERF is less than the IRF. Figure 3 shows the
 298 normalized time-integrated rapid adjustments (divided by the magnitude of the time-
 299 integrated IRF so the sign is preserved) averaged over the different subsets of eruptions. On
 300 average, the positive rapid adjustments reduce the volcanic forcing by 20% and are
 301 dominated by a positive SW cloud adjustment (Figure 3g) driven by cloud changes that
 302 reduce reflected SW radiation. It is not possible with our model diagnostics to attribute this
 303 adjustment to specific cloud changes, but we do simulate a large reduction in high-level
 304 clouds consistent with studies that investigated cloud changes due to sulfate geoengineering
 305 (e.g., Krishnamohan et al., 2019; Kuebbeler et al., 2012; Visioni et al., 2018) and some
 306 smaller changes to low-level clouds (Figure S5). Our result agrees with that of Gregory et al.
 307 (2016) for SW cloud adjustments, who also investigated the radiative forcing from volcanic
 308 eruptions. Their study did not diagnose the LW cloud adjustment. We find a small negative
 309 LW adjustment from a reduction in cloud fraction (Figure 3h). In contrast, Schmidt et al.
 310 (2018) found a positive net aerosol-cloud adjustment following eruptions in CESM1-
 311 WACCM due to a positive LW aerosol-cloud interaction. This is further evidence that the
 312 sign and magnitude of aerosol-cloud interactions following volcanic eruptions remain highly
 313 uncertain and model dependent.

314 The remainder of the rapid adjustments are much smaller, although most are still
 315 statistically significant (Student's t-test; stars in Figure 3). The spatial signatures of the rapid
 316 adjustments are shown in Figures S6-S11. In general, the surface and tropospheric
 317 temperature adjustments are positive (i.e., surface and tropospheric cooling leads to a
 318 reduction in outgoing longwave radiation) and the stratospheric temperature adjustment is
 319 negative (i.e., stratospheric warming following longwave absorption by the sulfate aerosols
 320 leads to an increase in emissivity). The tropospheric temperature adjustment is strongest for
 321 the NH eruptions and weakest for the SH eruptions likely because of the greater proportion of
 322 land that can cool in the NH where the forcing occurs. The water vapor adjustment is both
 323 positive and negative but is generally not statistically significant except for summer
 324 eruptions. The water vapor adjustment reflects a balance between a decrease in tropospheric
 325 water vapor due to cooling and an increase in stratospheric water vapor due to aerosol heating
 326 (Dessler et al., 2013; Krishnamohan et al., 2019). The surface albedo adjustment is also
 327 positive, reflecting changes in aerosol optical depth, snow cover and clouds.

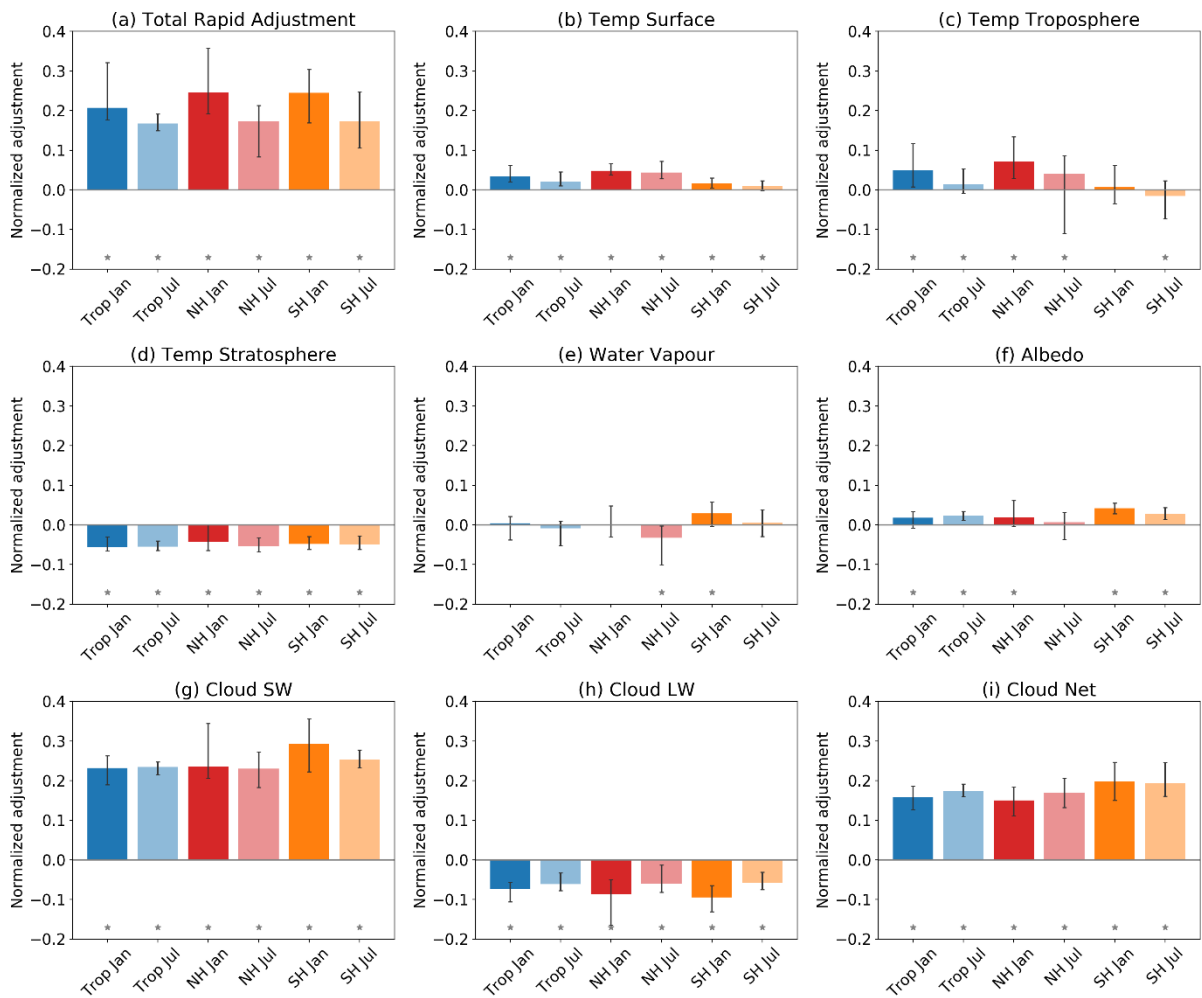
328 The differences in the relationship between SAOD and ERF are predominantly due to
 329 the differences in the magnitude of IRF outlined in section 3.1. However, we also find some
 330 differences in the normalized total rapid adjustments and hence the ERF to IRF ratio,
 331 depending on the ESPs, and the time since an eruption. For example, the proportion of the
 332 IRF that is offset by the positive rapid adjustments is consistently larger for eruptions
 333 occurring in January, regardless of the latitude (Figure 3a). For the January eruptions, the
 334 rapid adjustments are ~23% of the IRF and ~17% of the IRF for the July eruptions. This is
 335 mainly driven by the surface and tropospheric temperature adjustments, which are stronger
 336 for the January eruptions (Figures 3b-c). Spatial plots of the tropospheric temperature
 337 adjustment for January eruptions (Figures S6, S8, S10) show a large positive adjustment near

338 Greenland, suggesting that changes in circulation are driving this adjustment for eruptions in
 339 both hemispheres.

340

341 The relative role of the total rapid adjustments (RA) also increases over time (see
 342 Figure S12). For January eruptions RA/IRF is 19% in year 1, 24% in year 2 and 48% in year
 343 3, although the forcing and rapid adjustments are extremely small and noisy in year 3 and are
 344 therefore less important. The corresponding percentages for July eruptions are 16% (year 1)
 345 18% (year 2) and 25% (year 3). The relative importance of all RA changes in each year and
 346 in opposing directions and depends on the eruption month. The changing RA/IRF ratio is
 347 therefore not attributable to a single adjustment and likely changes over time because of
 348 different timescales and spatial patterns of the rapid adjustments that depend on the spatial
 349 and microphysical evolution of the aerosol.

350



351

352 **Figure 3.** Time-integrated global-mean rapid adjustments (a-i) averaged across the different
 353 eruption subsets. Rapid adjustments in each simulation were divided by the magnitude of the
 354 time-integrated global-mean IRF (keeping positive rapid adjustments positive). The total
 355 rapid adjustment is shown in Figure 3a and the remaining subplots show the breakdown of
 356 the total rapid adjustment into the contributing components. Error bars show the range in the
 357 rapid adjustments amongst the eruptions in each subset. Stars indicate where the adjustment
 358 is significant at the 95% confidence level according to a two-sided Student's t-test.

359 Conclusions

360 The conversion between global-mean volcanic SAOD and global-mean ERF is an
 361 important relationship to understand volcanic climate forcing efficiency, and required by
 362 simple climate models that continue to underpin IPCC assessments.

363 Previous studies have focused on a limited number of eruptions to determine the
 364 relationship between SAOD and volcanic radiative forcing. We have investigated this
 365 relationship across aerosol-climate model simulations of a very wide range of eruptions with
 366 different SO₂ emission magnitudes (10-100 Tg SO₂), latitudes (80°S-80°N), and for eruptions
 367 in January and July. We have shown that the SAOD to ERF relationship is non-unique and
 368 varies widely depending on the aerosol distribution and incoming solar radiation and
 369 consequently the time after an eruption, eruption season and eruption latitude. For eruption
 370 categories investigated here, forcing per unit of SAOD is weaker in the first year following an
 371 eruption than in years 2 and 3, is stronger for tropical eruptions than extratropical eruptions
 372 and stronger for winter eruptions than summer eruptions.

373 We find that the average scaling factor (across all eruption categories) between SAOD
 374 and ERF is $-17.0 \pm 0.2 \text{ W m}^{-2}$, which is considerably lower than the factor of -26 W m^{-2} per
 375 unit SAOD used by IPCC AR5. In our study this is because positive rapid adjustments
 376 dominated by a positive shortwave cloud adjustment act to reduce the volcanic forcing; the
 377 ERF is on average 20% less than the instantaneous radiative forcing (IRF). Total rapid
 378 adjustments are on average stronger for January eruptions regardless of eruption latitude,
 379 offsetting ~23% of the IRF compared to ~17% for the July eruptions due to a larger surface
 380 and tropospheric temperature adjustment that occurs for January eruptions. Our results
 381 provide evidence that uncertainty in volcanic forcing estimates based on volcanic SAOD and
 382 therefore volcanic climatic impacts is large. Our results also suggest that volcanic forcing has
 383 been previously overestimated, which has implications for transient energy balance
 384 calculations used to constrain the transient climate response and equilibrium climate
 385 sensitivity. For example, we find that the time-integrated volcanic ERF for eruptions between
 386 500 BCE and 1900 CE is around 20% less than that based on the IPCC AR5 scaling factor
 387 with resulting differences in peak global-mean surface cooling following the largest eruptions
 388 of up to 0.4°C.

389 We provide several conversions between global annual-mean volcanic SAOD (in the
 390 form of $1 - e^{-\text{SAOD}}$) and ERF (Figure 1, Table S1). These conversions do not account for all
 391 variability we find in the relationship between SAOD and ERF, and which may also vary
 392 depending on the model used and atmospheric background state, but provide a considerable
 393 improvement on the single scaling factor as used by IPCC AR5.

394
395

396 **Acknowledgments**

397 We thank Jonathan Gregory for valuable and insightful comments and feedback,
 398 which greatly improved this work. We also thank Matthew Toohey for providing the
 399 EVA(2k) simulations with no background aerosol included.

400 L.M. and A.S. are funded by the U.K. Natural Environment Research Council
 401 (NERC) via the “Vol-Clim” grant (NE/S000887/1). P.M.F, C.J.S and T.A. acknowledge
 402 support from the European Union’s Horizon 2020 grant agreement number 820829
 403 (CONSTRAIN). P.M.F, C.J.S and A.S. also acknowledge funding from NERC under project
 404 NE/N006038/1 (SMURPHS). C.J.S was additionally supported by a NERC/IIASA
 405 Collaborative Research Fellowship (NE/T009381/1). T.J.A. acknowledges funding from the
 406 Royal Society through a Newton International Fellowship (grant number NIF\R1\180809)
 407 and from the Sidney Sussex college through a Junior Research Fellowship. T.A was
 408 supported by the Met Office Hadley Centre Climate Programme funded by Department for
 409 Business, Energy and Industrial Strategy (BEIS) and Department for Environment, Food and
 410 Rural Affairs (Defra). This work used the ARCHER UK National Supercomputing Service
 411 (<http://www.archer.ac.uk>) and JASMIN super-data cluster (doi:10.1109/
 412 BigData.2013.6691556), via the Centre for Environmental Data Analysis (CEDA).

413 Summary model data are currently being uploaded to the CEDA archive and are in the
 414 supporting information (Tables S2-S15).

415
 416

417 **References**

- 418
 419 Andersson, S. M., Martinsson, B. G., Vernier, J. P., Friberg, J., Brenninkmeijer, C. A. M., Hermann, M., et al.
 420 (2015). Significant radiative impact of volcanic aerosol in the lowermost stratosphere. *Nature*
 421 *Communications*, 6. 10.1038/ncomms8692
 422 Aubry, T. J., Toohey, M., Marshall, L., Schmidt, A., & Jellinek, A. M. (2020). A new volcanic stratospheric
 423 sulfate aerosol forcing emulator (EVA_H): Comparison with interactive stratospheric aerosol models.
 424 *Journal of Geophysical Research: Atmospheres*, 125, e2019JD031303. 10.1029/2019JD031303
 425 Crowley, T., & Unterman, M. B. (2013). Technical details concerning development of a 1200 yr proxy index for
 426 global volcanism. *Earth System Science Data*, 5(1), 187-197. 10.5194/essd-5-187-2013
 427 Dessler, A. E., Schoeberl, M. R., Wang, T., Davis, S. M., & Rosenlof, K. H. (2013). Stratospheric water vapor
 428 feedback. *Proceedings of the National Academy of Sciences*, 110(45), 18087.
 429 10.1073/pnas.1310344110
 430 Edwards, J. M., & Slingo, A. (1996). Studies with a flexible new radiation code .1. Choosing a configuration for
 431 a large-scale model. *Quarterly Journal of the Royal Meteorological Society*, 122(531), 689-719.
 432 10.1002/qj.49712253107
 433 Forster, P. M., Andrews, T., Good, P., Gregory, J. M., Jackson, L. S., & Zelinka, M. (2013). Evaluating adjusted
 434 forcing and model spread for historical and future scenarios in the CMIP5 generation of climate
 435 models. *Journal of Geophysical Research: Atmospheres*, 118(3), 1139-1150. 10.1002/jgrd.50174
 436 Forster, P. M., Richardson, T., Maycock, A. C., Smith, C. J., Samset, B. H., Myhre, G., et al. (2016).
 437 Recommendations for diagnosing effective radiative forcing from climate models for CMIP6. *Journal*
 438 *of Geophysical Research: Atmospheres*, 121(20), 12,460-412,475. 10.1002/2016JD025320
 439 Gao, C., Robock, A., & Ammann, C. (2008). Volcanic forcing of climate over the past 1500 years: An improved
 440 ice core-based index for climate models. *Journal of Geophysical Research-Atmospheres*, 113(D23).
 441 Article. 10.1029/2008jd010239
 442 Gregory, J. M., Andrews, T., Ceppi, P., Mauritsen, T., & Webb, M. J. (2019). How accurately can the climate
 443 sensitivity to CO2 be estimated from historical climate change? *Climate Dynamics*. 10.1007/s00382-
 444 019-04991-y
 445 Gregory, J. M., Andrews, T., Good, P., Mauritsen, T., & Forster, P. M. (2016). Small global-mean cooling due
 446 to volcanic radiative forcing. *Climate Dynamics*, 47(12), 3979-3991. 10.1007/s00382-016-3055-1
 447 Guo, S., Rose, W. I., Bluth, G. J. S., & Watson, I. M. (2004). Particles in the great Pinatubo volcanic cloud of
 448 June 1991: The role of ice. *Geochemistry Geophysics Geosystems*, 5. 10.1029/2003gc000655

- 449 Hansen, J., Sato, M., Ruedy, R., Nazarenko, L., Lacis, A., Schmidt, G. A., et al. (2005). Efficacy of climate
450 forcings. *Journal of Geophysical Research-Atmospheres*, *110*(D18). Review. 10.1029/2005jd005776
- 451 Haustein, K., Otto, F. E. L., Venema, V., Jacobs, P., Cowtan, K., Hausfather, Z., et al. (2019). A Limited Role
452 for Unforced Internal Variability in Twentieth-Century Warming. *Journal of Climate*, *32*(16), 4893-
453 4917. 10.1175/jcli-d-18-0555.1
- 454 Krishnamohan, K. P. S. P., Bala, G., Cao, L., Duan, L., & Caldeira, K. (2019). Climate system response to
455 stratospheric sulfate aerosols: sensitivity to altitude of aerosol layer. *Earth Syst. Dynam.*, *10*(4), 885-
456 900. 10.5194/esd-10-885-2019
- 457 Kuebbeler, M., Lohmann, U., & Feichter, J. (2012). Effects of stratospheric sulfate aerosol geo-engineering on
458 cirrus clouds. *Geophysical Research Letters*, *39*(23). 10.1029/2012gl053797
- 459 Landwehrs, J. P., Feulner, G., Hofmann, M., & Petri, S. (2020). Climatic fluctuations modeled for carbon and
460 sulfur emissions from end-Triassic volcanism. *Earth and Planetary Science Letters*, *537*, 116174.
461 doi.org/10.1016/j.epsl.2020.116174
- 462 Larson, E. J. L., & Portmann, R. W. (2016). A Temporal Kernel Method to Compute Effective Radiative
463 Forcing in CMIP5 Transient Simulations. *Journal of Climate*, *29*(4), 1497-1509. 10.1175/JCLI-D-15-
464 0577.1
- 465 Mann, G. W., Carslaw, K. S., Spracklen, D. V., Ridley, D. A., Manktelow, P. T., Chipperfield, M. P., et al.
466 (2010). Description and evaluation of GLOMAP-mode: a modal global aerosol microphysics model for
467 the UKCA composition-climate model. *Geoscientific Model Development*, *3*(2), 519-551.
468 10.5194/gmd-3-519-2010
- 469 Manners, J., Edwards, J. M., Hill, P., & Thelen, J. C. (2015). *SOCRATES (Suite Of Community Radiative*
470 *Transfer codes based on Edwards and Slingo) technical guide*. Met Office, UK.
- 471 Marshall, L., Johnson, J. S., Mann, G. W., Lee, L., Dhomse, S. S., Regayre, L., et al. (2019). Exploring How
472 Eruption Source Parameters Affect Volcanic Radiative Forcing Using Statistical Emulation. *Journal of*
473 *Geophysical Research: Atmospheres*, *124*, 964–985. 10.1029/2018JD028675
- 474 Marshall, L., Schmidt, A., Toohey, M., Carslaw, K. S., Mann, G. W., Sigl, M., et al. (2018). Multi-model
475 comparison of the volcanic sulfate deposition from the 1815 eruption of Mt. Tambora. *Atmospheric*
476 *Chemistry and Physics*, *18*(3), 2307-2328. 10.5194/acp-18-2307-2018
- 477 Millar, R. J., Nicholls, Z. R., Friedlingstein, P., & Allen, M. R. (2017). A modified impulse-response
478 representation of the global near-surface air temperature and atmospheric concentration response to
479 carbon dioxide emissions. *Atmos. Chem. Phys.*, *17*(11), 7213-7228. 10.5194/acp-17-7213-2017
- 480 Myhre, G., Shindell, D., Bréon, F.-M., Collins, W., Fuglestedt, J., Huang, J., et al. (2013). Anthropogenic and
481 Natural Radiative Forcing. In T. F. Stocker, D. Qin, G. K. Plattner, M. Tignor, S. K. Allen, J.
482 Boschung, A. Nauels, Y. Xia, V. Bex, & P. M. Midgley (Eds.), *Climate Change 2013: The Physical*
483 *Science Basis. Contribution of Working Group I to the Fifth Assessment Report of the*
484 *Intergovernmental Panel on Climate Change*. Cambridge, United Kingdom and New York, NY, USA.:
485 Cambridge University Press.
- 486 Schmidt, A., Mills, M. J., Ghan, S., Gregory, J. M., Allan, R. P., Andrews, T., et al. (2018). Volcanic Radiative
487 Forcing From 1979 to 2015. *Journal of Geophysical Research: Atmospheres*, *123*(22), 12,491-412,508.
488 10.1029/2018jd028776
- 489 Schurer, A. P., Hegerl, G. C., Mann, M. E., Tett, S. F. B., & Phipps, S. J. (2013). Separating Forced from
490 Chaotic Climate Variability over the Past Millennium. *Journal of Climate*, *26*(18), 6954-6973.
491 10.1175/jcli-d-12-00826.1
- 492 Shell, K. M., Kiehl, J. T., & Shields, C. A. (2008). Using the Radiative Kernel Technique to Calculate Climate
493 Feedbacks in NCAR's Community Atmospheric Model. *Journal of Climate*, *21*(10), 2269-2282.
494 10.1175/2007JCLI2044.1
- 495 Sherwood, S. C., Bony, S., Boucher, O., Bretherton, C., Forster, P. M., Gregory, J. M., & Stevens, B. (2015).
496 Adjustments in the Forcing-Feedback Framework for Understanding Climate Change. *Bulletin of the*
497 *American Meteorological Society*, *96*(2), 217-228. 10.1175/BAMS-D-13-00167.1
- 498 Sigl, M., Winstrup, M., McConnell, J. R., Welten, K. C., Plunkett, G., Ludlow, F., et al. (2015). Timing and
499 climate forcing of volcanic eruptions for the past 2,500 years. *Nature*, *523*(7562), 543–549.
500 10.1038/nature14565
- 501 Smith, C. J., Forster, P. M., Allen, M., Fuglestedt, J., Millar, R. J., Rogelj, J., & Zickfeld, K. (2019).
502 Current fossil fuel infrastructure does not yet commit us to 1.5 °C warming. *Nature Communications*,
503 *10*(1), 101. 10.1038/s41467-018-07999-w
- 504 Smith, C. J., Forster, P. M., Allen, M., Leach, N., Millar, R. J., Passerello, G. A., & Regayre, L. A. (2018a).
505 FAIR v1.3: a simple emissions-based impulse response and carbon cycle model. *Geosci. Model Dev.*,
506 *11*(6), 2273-2297. 10.5194/gmd-11-2273-2018

- 507 Smith, C. J., Kramer, R. J., Myhre, G., Forster, P. M., Soden, B. J., Andrews, T., et al. (2018b). Understanding
508 Rapid Adjustments to Diverse Forcing Agents. *Geophysical Research Letters*, *45*(21), 12,023-012,031.
509 10.1029/2018GL079826
- 510 Smith, C. J., Kramer, R. J., & Sima, A. (2020). The HadGEM3-GA7.1 radiative kernel: the importance of a
511 well-resolved stratosphere. *Earth Syst. Sci. Data Discuss.*, *2020*, 1-16. 10.5194/essd-2019-254
- 512 Soden, B. J., Held, I. M., Colman, R., Shell, K. M., Kiehl, J. T., & Shields, C. A. (2008). Quantifying Climate
513 Feedbacks Using Radiative Kernels. *Journal of Climate*, *21*(14), 3504-3520. 10.1175/2007JCLI2110.1
- 514 Stoffel, M., Khodri, M., Corona, C., Guillet, S., Poulain, V., Bekki, S., et al. (2015). Estimates of volcanic-
515 induced cooling in the Northern Hemisphere over the past 1,500 years. *Nature Geoscience*, *8*(10), 784-
516 788. 10.1038/ngeo2526
- 517 Taylor, K. E., Crucifix, M., Braconnot, P., Hewitt, C. D., Doutriaux, C., Broccoli, A. J., et al. (2007). Estimating
518 Shortwave Radiative Forcing and Response in Climate Models. *Journal of Climate*, *20*(11), 2530-2543.
519 10.1175/JCLI4143.1
- 520 Timmreck, C., Mann, G. W., Aquila, V., Hommel, R., Lee, L. A., Schmidt, A., et al. (2018). The Interactive
521 Stratospheric Aerosol Model Intercomparison Project (ISA-MIP): motivation and experimental design.
522 *Geoscientific Model Development*, *11*(7), 2581-2608. 10.5194/gmd-11-2581-2018
- 523 Toohey, M., Kruger, K., Niemeier, U., & Timmreck, C. (2011). The influence of eruption season on the global
524 aerosol evolution and radiative impact of tropical volcanic eruptions. *Atmospheric Chemistry and
525 Physics*, *11*(23), 12351-12367. 10.5194/acp-11-12351-2011
- 526 Toohey, M., Kruger, K., & Timmreck, C. (2013). Volcanic sulfate deposition to Greenland and Antarctica: A
527 modeling sensitivity study. *Journal of Geophysical Research-Atmospheres*, *118*(10), 4788-4800.
528 10.1002/jgrd.50428
- 529 Toohey, M., & Sigl, M. (2017). Volcanic stratospheric sulfur injections and aerosol optical depth from 500 BCE
530 to 1900 CE. *Earth System Science Data*, *9*(2), 809-831. 10.5194/essd-9-809-2017
- 531 Toohey, M., Stevens, B., Schmidt, H., & Timmreck, C. (2016). Easy Volcanic Aerosol (EVA v1.0): an idealized
532 forcing generator for climate simulations. *Geoscientific Model Development*, *9*(11), 4049-4070.
533 10.5194/gmd-9-4049-2016
- 534 Visioni, D., Pitari, G., di Genova, G., Tilmes, S., & Cionni, I. (2018). Upper tropospheric ice sensitivity to
535 sulfate geoengineering. *Atmos. Chem. Phys.*, *18*(20), 14867-14887. 10.5194/acp-18-14867-2018
- 536 Walters, D. N., Williams, K. D., Boutle, I. A., Bushell, A. C., Edwards, J. M., Field, P. R., et al. (2014). The
537 Met Office Unified Model Global Atmosphere 4.0 and JULES Global Land 4.0 configurations.
538 *Geoscientific Model Development*, *7*(1), 361-386. 10.5194/gmd-7-361-2014
- 539 Wetherald, R. T., & Manabe, S. (1988). Cloud Feedback Processes in a General Circulation Model. *Journal of
540 the Atmospheric Sciences*, *45*(8), 1397-1416. 10.1175/1520-0469(1988)045<1397:CFPIAG>2.0.CO;2
- 541 Zanchettin, D., Khodri, M., Timmreck, C., Toohey, M., Schmidt, A., Gerber, E. P., et al. (2016). The Model
542 Intercomparison Project on the climatic response to Volcanic forcing (VolMIP): experimental design
543 and forcing input data for CMIP6. *Geoscientific Model Development*, *9*(8), 2701-2719. 10.5194/gmd-9-
544 2701-2016
- 545
- 546